

pubs.acs.org/JACS Article

Giant Gateable Osmotic Power Generation from a Goldilocks Two-Dimensional Polymer

Baorui Cheng, Yu Zhong, Yuqing Qiu, Suriyanarayanan Vaikuntanathan, and Jiwoong Park*



Cite This: J. Am. Chem. Soc. 2023, 145, 5261-5269



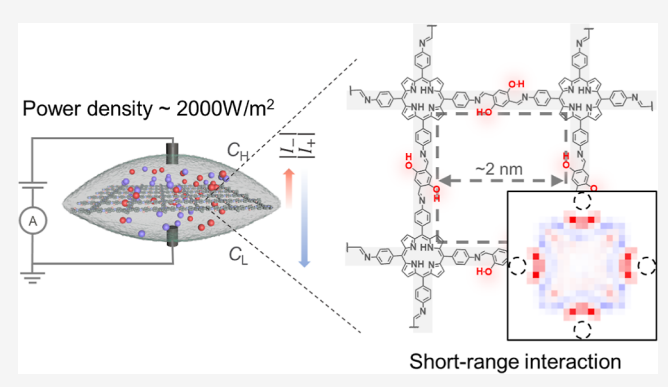
ACCESS

III Metrics & More

Article Recommendations

Supporting Information

ABSTRACT: Generating electricity from a salinity gradient, known as osmotic power, provides a sustainable energy source, but it requires precise nanoscale control of membranes for maximum performance. Here, we report an ultrathin membrane, where molecule-specific short-range interactions enable giant gateable osmotic power with a record high power density (2 kW/m² for 1 M||1 mM KCl). Our membranes are charge-neutral two-dimensional polymers synthesized from molecular building blocks and operate in a Goldilocks regime that simultaneously maintains high ionic conductivity and permselectivity. Molecular dynamics simulations quantitatively confirm that the functionalized nanopores are small enough for high selectivity through short-range ion—membrane interactions and large enough for fast cross-



membrane transport. The short-range mechanism further enables reversible gateable operation, as demonstrated by polarity switching of osmotic power with additional gating ions.

■ INTRODUCTION

Osmotic power or "blue energy", is emerging as a new form of renewable energy suitable for a wide range of applications including megawatt power plants at estuaries, medical implant devices, and microscopic iontronics. 1-4 The key component to osmotic power generation is a permselective membrane that enables selective transport of cations over anions (or vice versa), which leads to a higher current $|I^{+}|$ for one kind of ions over the other $|I^-|$ (Figure 1A). The requirement for high osmotic power generation is straightforward in principle: the membrane needs to maximize the product of net ionic current $(I_o = |I^+ + I^-|)$ and the voltage $(V_o;$ determined by permselectivity $|I^+/I^-|$) across the membrane for a given concentration gradient ($\Delta = C_H/C_L$, where C_H and C_L are the ionic concentrations on either side of the membrane). Therefore, an ideal permselective membrane should have both large ionic conductivity and high selectivity, although existing membranes generally increase one aspect at the expense of the other.

Recently, nanoporous two-dimensional (2D) materials have emerged as a platform with exceptional ionic conductivity because of their nanoscale thickness and high porosity. However, despite significant improvements in power density, the permselectivity of these membranes still has much to be improved. For high permselectivity, there are two principal driving forces: long-range and short-range interactions. A well-known example of the former is charge—charge Coulomb interactions. When a membrane is electrically charged, it attracts/repels the ions of the opposite/same charge, therefore

creating a concentration imbalance and permselectivity. This effect, however, becomes ineffective in nanoporous membranes with reduced physical space (i.e., in membranes that are thinner and more porous) to accommodate charges because it relies on volumetric charge screening. 5,11–15 In contrast, shortrange interactions (Figure 1B) rely on the specific nature of pairwise interactions (e.g., hydrogen bonding, coordination, dipole-dipole) between the ions, membrane, and water molecules and become significant for membranes with smaller pore sizes (below a few nanometers). If an ion's binding energy to the membrane $(\varepsilon_{\rm bind})$ is larger than that to water $(\varepsilon_{\rm H,O})$, the ionic movement will slow down as the ion easily binds to the membrane (red ions, Figure 1B). On the other hand, if $\varepsilon_{\rm bind}$ < $\varepsilon_{\mathrm{H,O}}$, the ion prefers remaining fully hydrated (blue ions, Figure 1B, left) and therefore diffuses faster than the bound ions. This mechanism enables permselectivity with unique properties different from the long-range mechanism; it is effective for a charge-neutral membrane; the selectivity is determined by the binding strength rather than the charge polarity of the ion; and it can be further tuned by the

Received: December 2, 2022 Published: February 27, 2023





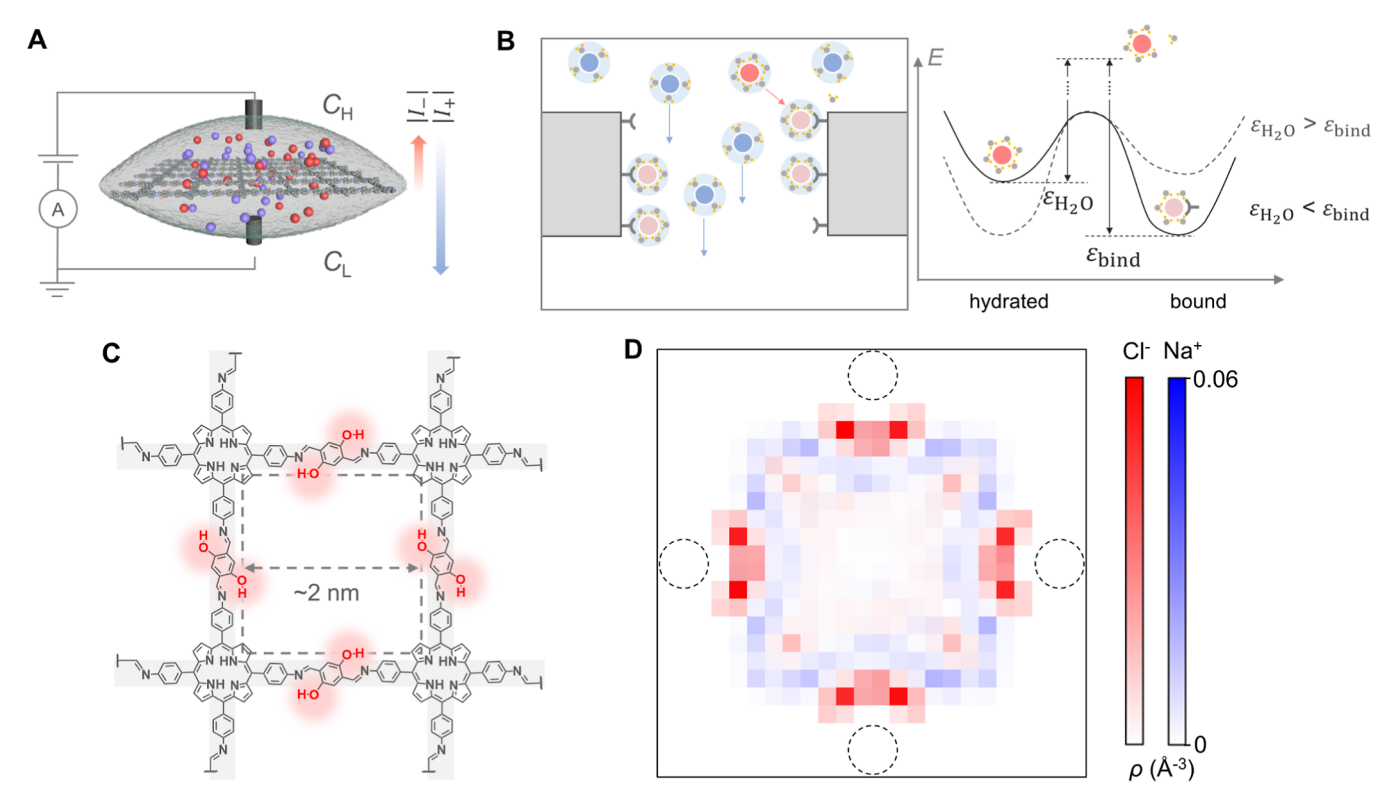


Figure 1. Osmotic power generation using 2DNP. (A) Schematic illustration of osmotic power generation using the permselective 2DNP membrane. (B) (Left) Illustration of permselectivity through pairwise short-range interaction and (right) the corresponding energy diagram sketch. (C) Structural backbone of the 2DNP membrane. (D) Cl^- (red) and Na^+ (blue) distribution within a single 2DNP (4-layer) nanopore calculated using CG-MD simulations. Center-to-center distance of edge carbon atoms is 2.25 nm, resulting in an open pore size of \sim 1.9 nm. The dashed circles indicate the positions of -OH groups, and each pixel is 1×1 Å 2 .

composition of ions and pore dimensions for advanced operations such as gated ionic transport and sensing. 16,17

Despite such advantages, there exist to date limited reports of high osmotic power generation primarily based on shortrange interactions. Ideally, such studies would require 2D nanoporous membranes with (a) high ionic conductance and permselectivity, (b) nanoscale pores with precisely known functional groups, and (c) a theoretical model based on specific short-range interactions predicting further performance optimization. Instead, permselectivities in previously reported nanoporous membranes, made of single-layer polycyclic aromatic hydrocarbons⁸ and ultrathin holey-graphene-like membranes, were all attributed to the Coulomb screening effect from the membrane surface charges. This also includes recent reports of high-power membranes showing opposite permselectivities despite very similar imine-linked porphyrin backbones. 10,18 This apparent discrepancy and the nanoscale pore sizes of these membranes suggest that the short-range interactions may play an important role in explaining these previous studies and further development.

Here, we report an ultrathin 2D nanoporous polymer (2DNP) membrane, where short-range interactions enable giant gateable osmotic power generation. Our study, including both experiments and simulations, shows that our 2DNP membrane meets all of the requirements listed above: it demonstrates high ionic conductance thanks to nanoscale thickness and large nanopore density; its pores are precisely defined through bottom-up synthesis; and despite the chargeneutral structure, it shows a high permselectivity and osmotic power densities. Molecular dynamics (MD) simulations explain the high permselectivity and identify the optimal

"Goldilocks" zone for the nanopore size. Furthermore, the short-range selectivity mechanism enables new functionalities, including ion-gated switching of osmotic power.

■ RESULTS AND DISCUSSION

Membrane Design and Device Fabrication. The design of our 2DNP membrane is illustrated in Figure 1C. The iminelinked backbone results in a high density of ~2 nm nanopores (~2.5 nm center-to-center distance between neighboring pores) that are decorated by phenolic -OH groups introduced through one of the monomers. Here, -OH, one of the most common functional groups, is specifically chosen for two reasons: (i) at moderate pH conditions (5-8), -OH is virtually free of deprotonation due to its large pKa (~10) and leaves the 2DNP charge neutral and (ii) due to the large polarity and hydrogen bonding capability, it can bind strongly to various ions, with $\varepsilon_{\mathrm{OH}}$, the ion–OH binding energy, comparable to $\varepsilon_{\rm H,O}$, the ion–water binding energy (Table S1). As an important example, the previous studies showed that Clbinds more strongly to -OH (i.e., $\varepsilon_{OH} > \varepsilon_{H,O}$), ^{19,20} while Na⁺ prefers binding to a water molecule $(\epsilon_{\rm OH} < \epsilon_{\rm H_2O})^{21,22}$ Such binding preferences make -OH groups play an important role in permselective ion transport. This is clearly demonstrated by our coarse-grained molecular dynamic (CG-MD) simulations, shown in Figure 1D. It plots the density distribution of Na+ (blue color) and Cl⁻ (red) during the diffusion process across a membrane with ∼2 nm nanopores decorated by −OH (dotted circles). Clear patterns emerge: while Cl⁻ is strongly localized near the -OH groups, Na⁺ stays away from -OH.

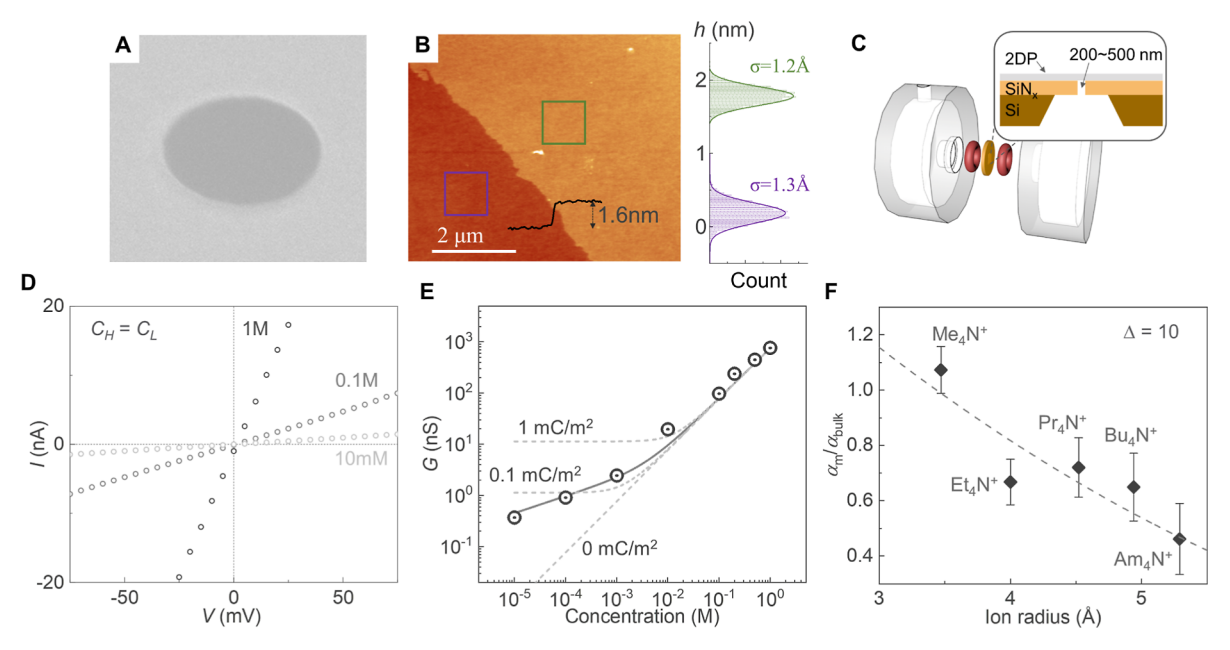


Figure 2. Fabrication and characterization of the 2DNP membranes with high ionic conductivity. (A) SEM image of 2DNP suspended over a 2 μ m hole in the carbon film. (B) (Left) AFM image of 2DNP transferred on a SiO₂/Si substrate. A line profile across the 2DNP edge is overlayed. (Right) Height histograms for the corresponding areas in the AFM on the left (purple: SiO₂/Si substrate, green: 2DNP). (C) Fabrication of 2DNP microfluidic devices. (D) I-V responses of a representative 2DNP membrane with different salt concentrations ($C_H = C_L$). (E) Conductance of the 2DNP membrane in (D) at different KCl concentrations. The dashed lines are calculated for different constant surface charge densities, and the solid line is the best fit of the data to a variable surface charge model. (F) Relative mobility ratios of different tetraalkylammonium cations to Cl⁻ (normalized by their mobilities in bulk solutions). The dashed line is the best fit to the data using a hydrodynamic model. The extracted pore size from the fit is ~1.9 nm.

This indicates a preferential binding of Cl⁻ to the -OH groups, enabling selective transport of Na⁺ over Cl⁻.

Our 2DNP membrane was synthesized using a recently developed interfacial synthesis technique named laminar assembly polymerization (LAP).²³ 2,5-Dihydroxyterephthalaldehyde (TPA-OH) and 5,10,15,20-tetrakis(4-aminophenyl)-21H,23H-porphine (TAPP) were crosslinked through a Schiffbase reaction at a pentane/water interface to form the designed 2DNP membranes. The absorption spectrum of the membrane shows a strong peak from the porphyrin Soret band (~440 nm), and the formation of an imine linkage was confirmed by Fourier-transform infrared (FTIR) spectroscopy (Figures S1 and S2), although no X-ray or electron diffraction data could be collected. The synthesized 2DNP membrane is optically homogeneous over a cm-scale and mechanically robust. As a result, the membrane can be transferred to various substrates and suspended over micron-sized holes (Figures 2A and S3). The 2DNP membrane has a uniform thickness of less than 2 nm (3–4 layers) and a smooth surface with roughness (\sim 0.1 nm) comparable to that of the underlying SiO₂/Si substrate, as measured using atomic force microscopy (AFM) (Figures 2B and **S4**).

High Cross-Membrane Ionic Conductivity. For ion-transport measurements, customized microfluidic devices (illustrated in Figure 2C) integrating a 2DNP membrane (diameter between 200 and 500 nm) were fabricated, and the current–voltage (I-V) characteristics were collected using a pair of Ag/AgCl electrodes. The ionic concentrations of the solutions on either side of the membrane were controlled independently $(C_{\rm H}$ and $C_{\rm L})$, generating a concentration gradient $\Delta = C_{\rm H}/C_{\rm L}$, ranging between 1 and 1000.

Figure 2D shows I-V curves measured from a representative device using KCl solutions of three different concentrations

(C; $\Delta = 1$). The ionic conductance (G) of the membrane, measured from the slope of these linear I-V curves, is plotted at different C values in Figure 2E. It shows that G monotonically decreases with C; at higher C (>10 mM), Gdecreases linearly with C, whereas the dependence is sublinear at lower values of C. Such behavior is significantly different from that of an electrically charged membrane, where G remains constant at low salt concentrations as the ionic conductance is dominated by surface charges.^{6,24,25} For comparison, G versus C curves (dashed lines) expected for three different surface charges (1, 0.1, and 0 mC/m²) are shown in Figure 2E. In contrast, our data do not show a constant minimum; instead, they agree well with a variable surface charge model where G scales with $C^{1/3}$ at low concentrations (solid line).²⁶ This behavior is related to the adsorption of charged species onto a neutral surface, consistent with the charge-neutral structure of our 2DNP membrane. Our data also confirm that the 2DNP membrane is highly permeable to ions. The areal ionic conductance G/A of our membrane reaches $\sim 500 \text{ S/cm}^2$ for 1 M KCl, where A is the membrane area defined by the aperture of the SiN_x support (Figure S5). This is one of the highest values reported to date for osmotic power membranes (Table S2).

The pore size of the 2DNP membrane was estimated by measuring the transmembrane conductance of a series of tetraalkylammonium chlorides $[(C_nH_{2n+1})_4N]Cl$ with increasing alkyl chain lengths (n=1-5). Thanks to their small sizes (~1 nm in diameter) and the rigidity of the alkyl chains, the interaction between these ions and the 2DNP membrane is dominated by their ionic nature. Therefore, these ions allowed us to only increase the size of the cation without significantly affecting the ion–membrane interactions. As n increases, the cross-membrane mobility of the cation (α_m) will decrease

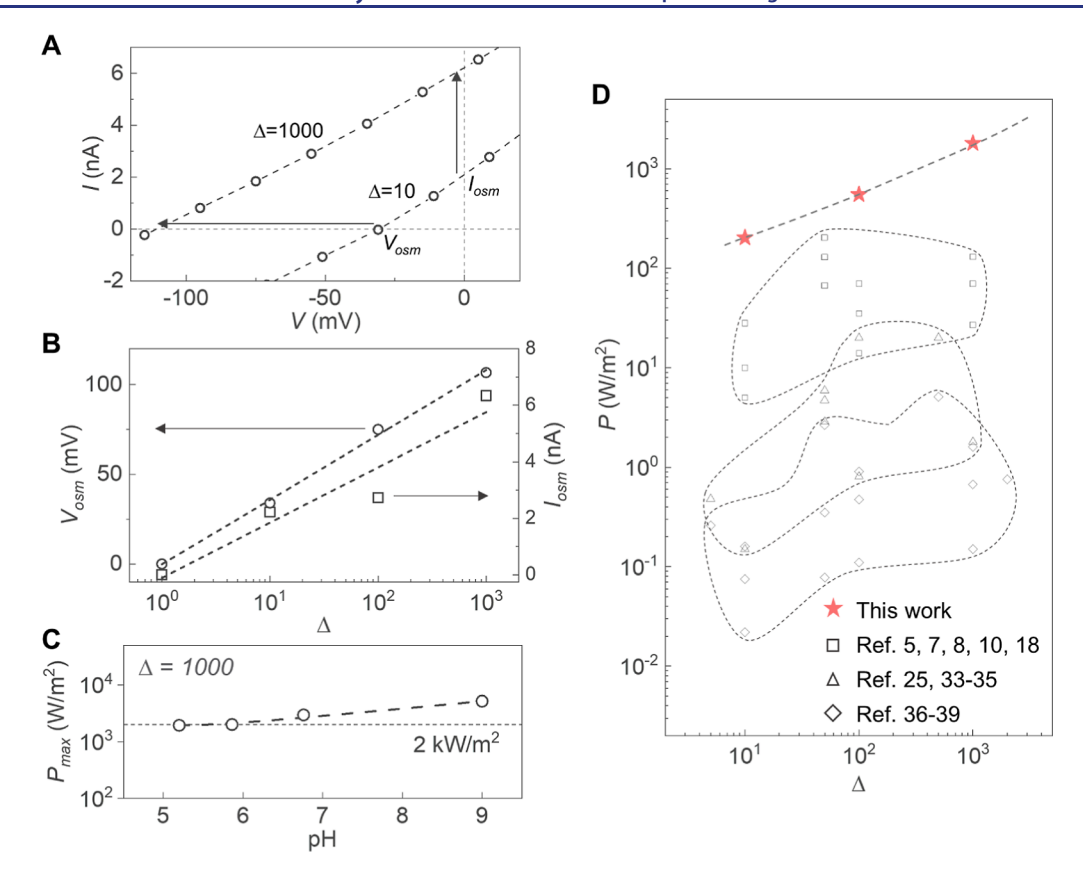


Figure 3. Giant osmotic power generation from 2DNP membrane. (A) I-V characteristics of a 2DNP membrane at $\Delta=10$ and $\Delta=1000$. (B) $V_{\rm osm}$ and $I_{\rm osm}$ of 2DNP measured at different Δ . (C) $P_{\rm max}$ of 2DNP membrane at different pH. (D) Comparison of power densities (P) for our 2DNP membrane (stars) and previously reported materials (squares for sub-10 nm nanoporous membranes, triangles for composite membranes, and rhombuses for polymeric membranes). All power densities are taken from ambient pH conditions.

relative to the bulk value ($\alpha_{\rm bulk}$) because of the small pore size and steric hindrance, and a simple hydrodynamic model predicts

$$\frac{\alpha_{\rm m}}{\alpha_{\rm bulk}} = c \left[1 - \frac{d}{D} \right]^2 \tag{1}$$

where $\alpha_{\rm m}$ and $\alpha_{\rm bulk}$ are each normalized using the mobilities of Cl⁻ as a reference, d is the diameter of the hydrated cations, D is the diameter of the pores, and c is a constant coefficient²⁷ (details in the Supporting Information). Figure 2F plots our experimental results (also see Figure S6). It shows a significant mobility reduction for larger cations; the best fit to the data (dashed curve) yields $D \sim 1.9$ nm, close to the designed size of the pores in our membrane (see Figure 1C). Therefore, the data in Figure 2 confirm that our 2D polymer membranes have properties closely following the molecular design, including nanoscale thickness, high porosity, and a nanoscale (~ 2 nm) pore size.

Giant Osmotic Power Generation. The ion-transport measurements conducted with a salinity gradient Δ (>1) confirm high permselectivity and osmotic power generation. Figure 3A shows I-V curves measured using our 2DNP membrane under Δ = 10 and 1000 with KCl solutions (also see Figure S7). Both curves show positive current $I_{\rm osm}$ at a zero bias, confirming the net osmotic current. The osmotic potential $V_{\rm osm}$ is measured from the x-intercept as it measures the external potential that stops the osmotic current; for example, we measured $V_{\rm osm} \sim 120$ mV for Δ = 1000. These observations are the results of permselective ion transport, and

the positive $I_{\rm osm}$ suggests that the membrane is cation-selective (see Figure S7, the circuit diagram). Other monovalent ionic solutions (i.e., NaCl, LiCl) also show similar properties (Figure S8), which are consistent with the short-range interaction mechanism introduced in Figure 1 and the preferential binding of Cl $^-$ to -OH. Both $V_{\rm osm}$ and $I_{\rm osm}$ increase with increasing Δ (Figure 3B), and the cation selectivity S of the membrane can be calculated using the equation 28

$$V_{\rm osm} = S \cdot \frac{RT}{zF} \cdot \ln \left(\frac{\gamma_{\rm H} C_{\rm H}}{\gamma_{\rm L} C_{\rm L}} \right) \tag{2}$$

where R is the universal gas constant, T is the ambient temperature (296 \pm 3 K), z is the charge valence of ions, F is the Faraday constant, and $\gamma_{\rm H}$ and $\gamma_{\rm L}$ are the activity coefficients of KCl at concentrations $C_{\rm H}$ and $C_{\rm L}$, respectively. S here is defined as $S=t_+-t_-$, where t_+ and t_- are the transference numbers of cations and anions across the membrane, respectively. From our data, we extract $S\sim0.6$, which is higher than the values for previously reported ultrathin 2D nanoporous membranes and single pores in 2D materials. 6,8,9,30

Because the I-V response is linear within the range of interest, the maximum power density $(P_{\rm max})$ of the membrane can be estimated as $P_{\rm max} = |I_{\rm osm} \cdot V_{\rm osm}|/4A$. For the device shown in Figure 3A, $P_{\rm max}$ is higher than 2 kW/m² at $\Delta = 1000$ (KCl solutions), setting a record for any reported porous membranes. When NaCl solutions were used for osmotic power generation in a more practical scenario, the 2DNP retained its high performance, and a power density of 350 W/

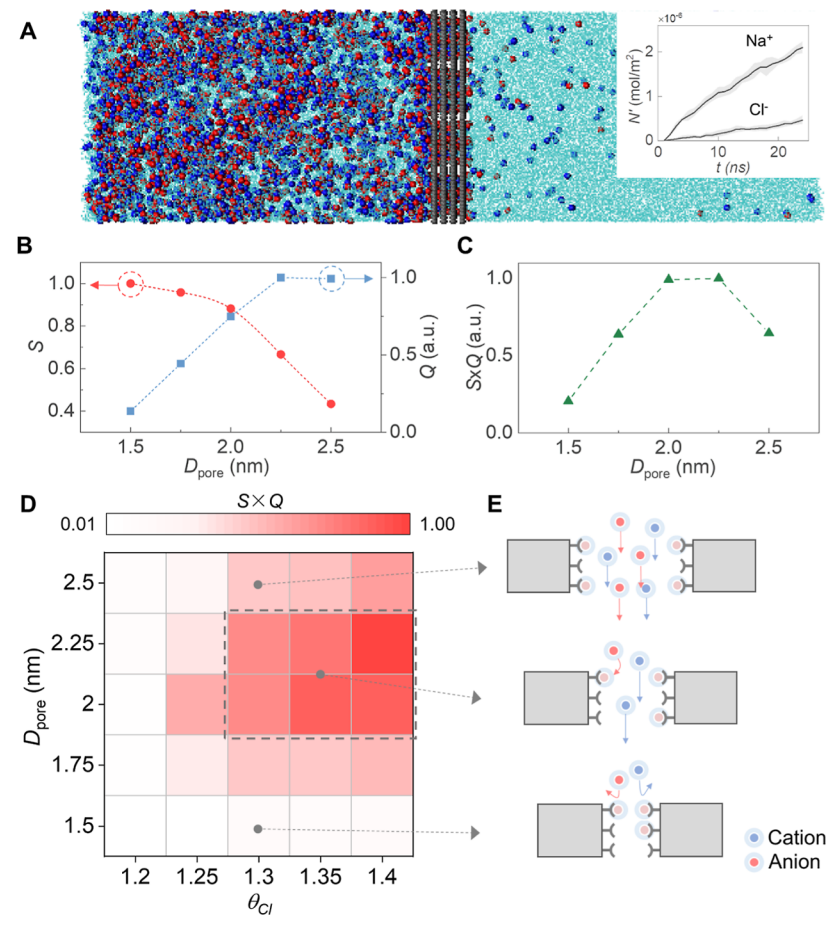


Figure 4. CG-MD simulated ion transport for optimal performance. (A) Snapshot of a representative simulation box used in CG-MD simulations. Inset: permeation of Na⁺ and Cl⁻ across the 2DNP membrane from the simulation. (B) S and Q as a function of D_{pore} ($\theta_{\text{Cl}} = 1.3$ and $\theta_{\text{Na}} = 0.8$). (C) Power output of the membrane (S × Q) as a function of D_{pore} ($\theta_{\text{Cl}} = 1.3$ and $\theta_{\text{Na}} = 0.8$). (D) Heatmap of S × Q for various combinations of θ_{Cl} and D_{pore} . (E) Schematics for ion transport at different pore sizes.

m² was achieved with artificial seawater and river water (0.5 M||0.01 M NaCl, Figure S9). Surprisingly, our 2DNP membrane can generate high osmotic power under a large range of pH (Figure 3C). This is drastically different from the case of charge-based membranes whose power performance is sensitive to pH, which modulates the membrane surface charge densities. The pH tolerance of power output from chargeneutral membranes is consistent with permselectivity based on short-range interactions, whose pairwise specificity is less sensitive to pH conditions.^{31,32} Figure 3D compares the osmotic power density reported from the previous studies with our results (red stars). It clearly shows that our 2DNP produces the highest power density at various Δ . 5,7,8,10,18,25,33-39 This high performance is a direct result of the combination of high ionic conductance and high permselectivity, without a strong trade-off between the two that limits the performance of many ultrathin membranes.^{5,6,8,10}

Our results demonstrate that both the permselectivity and ionic conductance can remain high because short-range interactions are effective even in a porous and ultrathin membrane. The effectiveness of this mechanism will change sensitively, depending on the nature and strength of each interacting pair and the precise geometry of the membrane system. For systematic optimization and advanced application developments, it is essential to understand the role of short-

range interactions and the nanopore dimensions during the ion transport.

MD Simulation for Optimization. For this, a CG-MD model incorporating realistic elements was developed. Ho,41 The essential structural features of the 2DNP are represented by porous carbon networks with $-\mathrm{OH}$ groups placed at all edges of each pore (Figure S10). Thereafter, a wide spectrum of membranes with different pore-to-pore distances D_{pore} (which is about 0.4 nm larger than the actual pore size due to the van der Waals volume of carbon atoms), 2DNP layer numbers n, and $\varepsilon_{\mathrm{OH}}$ were investigated using CG-MD simulations. A key parameter for the short-range interaction in our simulations is θ_{ion} , the ratio between a specific ion's binding energies to $-\mathrm{OH}$ versus $\mathrm{H_2O}$ ($\varepsilon_{\mathrm{OH}}/\varepsilon_{\mathrm{H_2O}}$), making the ion more likely to bind to $-\mathrm{OH}$ if $\theta_{\mathrm{ion}} > 1$. The previous studies indicate that $\theta_{\mathrm{Cl}} = 1.2 \sim 1.4$, whereas $\theta_{\mathrm{Na}} \sim 1.\frac{20.22}{1.20.22}$

Figure 4A is a snapshot taken from a simulation run (at t=25 ns) with parameters that closely represent our experiments ($D_{\rm pore}=2.25$ nm, n=4, and $\theta_{\rm Cl}=1.3$). High concentration of NaCl ($C_{\rm H}=3$ M) was introduced from one side to diffuse across the membrane to pure water, and the total number of permeated ions N' (normalized by the membrane area) was recorded as a function of time t. Figure 4A (inset) plots N'(t) for Na⁺ and Cl⁻ up to t=25 ns. $N'_{\rm Na}$ is larger than $N'_{\rm Cl}$ throughout the simulation with the Na⁺/Cl⁻ flux ratio ~ 5 ; this corresponds to $S\sim 0.7$, a value similar to our experimental

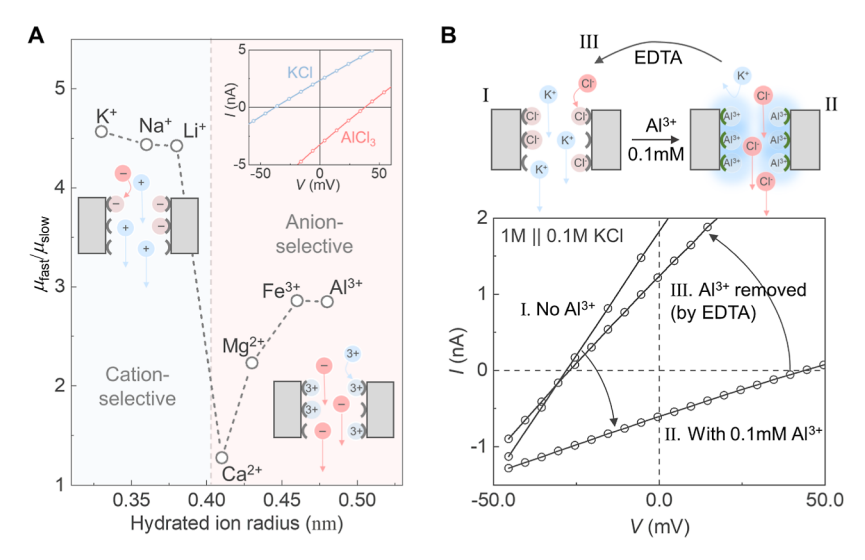


Figure 5. Gated switching of ion transport. (A) Mobility ratio $\mu_{\rm fast}/\mu_{\rm slow}$ for different metal chloride salt solutions with monovalent and multivalent cations. Inset: schematic diagrams for cation- (left) and anion- (right) selective transport and representative I-V characteristics (top) for KCl and AlCl₃; (B) (top) schematics and (bottom) I-V characteristics of Al³⁺-gated transport for KCl across the 2DNP membrane.

values (Figure 3A,B). While the actual permselective process may involve complicated effects such as the rearrangement of the hydration structure, our results in Figures 4 and S11 suggest that the relative binding strength θ_{ion} was the dominant factor in our tested conditions with both the polarity (i.e., cation selectivity) and the magnitude of the permselectivity reproduced by our simulations. However, as the pore sizes enter the sub-nanometer regime, we expect the hydration structure to become much more important and it must be considered for an accurate description.

In addition to S (which is proportional to the generated osmotic potential), the simulated N' is used to calculate Q, the net number of permeated charges (representing osmotic current). Studying how they change with D_{pore} or θ_{Cl} will quantify these parameters' effects on the osmotic power performance (proportional to $S \times Q$). First, our simulations show that, as θ_{Cl} is gradually reduced from 1.4 to 1.2, both S and Q decrease rapidly leading to vanishing osmotic power generation (Figure S12). This demonstrates the dominant role of the short-range -OH-Cl interaction for high power generation. Second, as D_{pore} increases from 1.5 to 2.5 nm, S continuously decreases (red points, Figure 4B). Q, on the other hand, initially increases but saturates at larger D_{pore} (blue points, Figure 4B), even though individual fluxes of Na⁺ and Cl⁻ continue to go up (Figure S13). This shows that there exists a narrow range for D_{pore} where both S and Q remain high for osmotic power generation, as confirmed by the plot of $S \times$ Q in Figure 4C. Below this range, D_{pore} is too small and the steric hindrance of the pore significantly blocks ionic transport leading to a small Q (Figure 4E, bottom); above this range, the short-range effect of the -OH-Cl binding is too diluted, leading to a small S (Figure 4E, top).

To maximize the osmotic power output from a membrane, it is essential to find a molecular design by employing an approach that systematically balances the steric hindrance and the short-range interactions. Our CG-MD simulations provide a powerful tool for identifying such designs. Figure 4D shows a 2D map of $S \times Q$ simulated as a function of θ_{Cl} (x-axis) and D_{pore} (y-axis), where we find the maximum $D_{\text{pore}} = 2.25 \text{ nm}$ and $\theta_{\rm Cl}$ = 1.4. In addition, it identifies a region of parameters (dashed boundary) with a high expected power (>70% of the

maximum), which can be considered a "Goldilocks zone". The power generation is efficient only for a very narrow range (\sim 0.5 nm) of $D_{\rm pore}$ and for $\theta_{\rm Cl}$ larger than 1.2. While a larger θ_{Cl} is preferred in general (Figure S12), the optimal value of D_{pore} slightly changes for each θ_{Cl} . Our simulations are consistent with several recent experimental results on membranes of similar structures 10,18,42 and confirm that the parameters for our 2DNP membranes are found within the Goldilocks zone, which explains the giant osmotic power shown in Figure 3. Significant permselectivity and osmotic power generation were also observed from a membrane with randomly positioned -OH groups (producing less long-range order), which indicates the generality of the short-range permselectivity (Figure S14). Although our MD simulation and experimental realization are based on specific -OH-ion (K⁺, Na⁺, and Cl⁻) interactions, the same paradigm can be applied to different functional groups (such as -NH2 and >C=O) and ionic species to realize the desired permselective ion transport in a wide range of systems (e.g., halogen salts, nitrate salts, and sulfate salts). This signifies the critical role of a precise molecular design for high-performance osmotic power generation as well as other membrane applications based on effective short-range interactions.

Gated Switching of Osmotic Power. One expected consequence of the short-range interaction mechanism is that the relative, not absolute, strengths of the binding energy determine which ions move faster across the membrane. For example, if we replace the monovalent cations (Li⁺, Na⁺, K⁺) with other ions that interact with -OH more strongly than (or as equally as) Cl-, the same 2DNP membrane could become anion-selective (or non-selective). This is indeed what we observed in our experiments. First, the I-V curve taken from our 2DNP membrane with AlCl₃ (upper inset, Figure 5A; red curve) shows a high osmotic power generation, but the polarity of the current and potential is reversed compared to that seen with KCl (blue), confirming the anion selectivity. Figure 5A plots the ratio of ionic mobilities for the faster ions (μ_{fast}) and slower ions (μ_{slow}) in different metal chloride salts. The high cation selectivity observed for monovalent cations (K+, Na+, and Li⁺) flips to high anion (Cl⁻) selectivity for multivalent cations (Mg²⁺, Fe³⁺, and Al³⁺), with Ca²⁺ producing nearly no

selectivity. The polarity switching and the ambipolar operation are consistent with the increased binding energy expected between polar -OH and multivalent ions. This makes Mg^{2+} , Fe^{3+} , or Al^{3+} (not Cl^-) bind more strongly to -OH, freeing Cl^- to move faster for anion selectivity (see the schematics, Figure 5A).

Moreover, preferential binding to certain cations enables gated switching of osmotic current, where a small number of ions that strongly bind to -OH drastically alters the transport of other ionic species, through the combination of steric and electrostatic interactions (see the schematics in Figure 5B). For example, adding Al3+ at a low concentration to KCl solution can saturate the binding sites of the nanopores. While this enables both K+ and Cl- to move freely without binding to -OH, the transport of Cl⁻ is preferred thanks to the Coulomb attraction between Cl⁻ and Al³⁺, as demonstrated by our experiments in Figure 5B. The addition of 0.1 mM Al³⁺ to KCl solutions (1 M||0.1 M) across a 2DNP membrane completely reverses the osmotic current and potential (I \rightarrow II). The original I-V curve was almost fully recovered when we regenerated the membrane using EDTA, a strong binding agent that removes Al^{3+} from the solution (II \rightarrow III). This series of experiments demonstrates that our 2DNP membranes operating with short-range interactions can generate giant gateable osmotic power, which can be used for ionic logic devices and sensitive ion detection. Additional experiments strongly suggest that these behaviors cannot be explained by the direct binding of multivalent (e.g., Al3+) ions at the porphyrin moieties, which usually requires much harsher conditions. First, similar gated switching of osmotic power was observed in a 2DNP made with Ni(II)-metalated porphyrin monomers (Figure S15). Second, 2DNP membranes made with Co(III)-metalated porphyrin monomers showed the same cation selectivity as in the 2H-TAPP membrane (Figure S16).

CONCLUSIONS

Our high-power osmotic membranes based on precise molecular design and MD-based optimization highlight the importance and exciting opportunity of chemical specificity and short-range interactions for permselective ion transport, which are often overlooked. The Goldilocks design principle also provides an additional guideline for future membrane design and optimization with both scientific and practical applications. For example, combining MD simulations with ab initio quantum chemical calculations 43 can generate a deeper understanding and more accurate predictions of crossmembrane ionic transport with atomistic details. While our 2DNP membrane demonstrates great potential for osmotic power generation, production and application of upscaled 2DNP membranes remain challenging despite recent advances. 8,18,23 A combination of precise molecular synthesis and new strategies for large-scale membrane fabrication and integration would be necessary to unleash the full potential of 2DNP membranes for high-performance osmotic power generation, water desalination/purification, and ion separation/extraction. 44-48

■ EXPERIMENTAL SECTION

 ${\bf Materials.}$ All chemicals were commercially available and used without further purification.

Synthesis of 2DNP Membranes. 20 μ L of 0.2 mM 2H-TAPP solution in pyridine/methanol (3:1 v/v) was introduced to a pentane/water interface using a syringe pump equipped with a 100 μ L syringe.

Aqueous TPA-OH solution was then introduced to the water phase to reach a final concentration of 5×10^{-5} M. The reaction system was then kept undisturbed for at least 12 h to allow complete polymerization. After the polymerization, the membrane was either drained onto a pre-submerged substrate or horizontally transferred from the top.

Ion Transport with Customized Microfluidic Devices. The 2DNP membrane was first transferred to a SiN_x support (50 nm) with a submicron hole at the center. The hole was created using a focused ion beam. The SiN_x support and the 2DNP membrane were then mounted between two customized acrylic compartments using silicone O-rings. A pair of Ag/AgCl electrodes was used to apply voltage and collect current from the microfluidic device. The voltage was supplied using a NI-6341 I/O device, while the current was first amplified by a SR-570 preamplifier and then analyzed by the I/O device. To eliminate the capacitance effect from SiN_x , in all I-Vmeasurements, a dc current was obtained by applying a constant voltage for at least 5 s and then using an exponential fit to get the steady-state current. The redox potentials of the Ag/AgCl electrodes were measured against a saturated Ag/AgCl reference electrode, and the contribution from their potential difference in the osmotic power generation was subtracted.

Characterizations. The UV-vis absorption spectrum of the 2DNP was taken by an Agilent Cary 5000 UV-vis-NIR spectrophotometer. FTIR spectra of the 2DNP membrane, TAPP powder, and TPA-OH powder were collected using a Thermo Nicolet NEXUS 670 with an attenuated total reflection (ATR) accessory. SEM imaging was done by either a Zeiss MERLIN field emission scanning electron microscope (FE-SEM) or a TESCAN LYRA3 FE-SEM (with FIB), both at 3 kV. Ambient AFM imaging was conducted using a Bruker Dimension Icon on 2DNP membranes transferred onto a SiO₂/Si substrate.

MD Simulation. MD simulations of the 2DNP membranes were performed with LAMMPS. 49 We modeled water with the monatomic water model mW.⁴¹ NaCl is modeled with a coarse-grained ion model⁴⁰ parameterized to reproduce the water's solvation of ions. The backbone of the two-dimensional polymer is represented by a chain of CH₂ groups with the Lennard-Jones interactions of the UA-OPLS⁵⁰ force field. The hydroxyl groups were modeled with mW. The interactions between the OPLS carbon and mW water/Na⁺/Cl⁻ ions were described by the same Lennard-Jones potential parameterized in a previous study to reproduce the surface tension of the nonane—water interface. The interaction between OH and mW water was the same as that between mW water molecules. We scaled the interactions between OH and Na+(Cl-) from the interactions between water and Na⁺(Cl⁻). We refer to this ratio of specific ion's binding energies to - OH versus H_2O $(\varepsilon_{\text{OH}}/$ $\varepsilon_{\text{H,O}})$ as the key parameter for the short-range interaction. We fixed the positions of the two-dimensional membrane, so that there were no effective interactions between OPLS carbon and OH groups in the membrane.

We performed MD simulations of ion transport across the twodimensional membrane. Each simulation box contained a 32 nm water slab and a membrane of 4 × 4 pores. The membrane was fully immersed in water, with a 16 nm water slab on each side (Figure 4A). The pore-to-pore distance $D_{\rm pore}$ ranged from 1.5 to 2.5 nm (Figure S10). Periodic boundary conditions were applied in the two directions parallel to the membrane (x & y), and fixed walls were placed at the ends of the simulation box along the z direction to confine the ions in the box. We placed 3 M of the ions on one side of the box and referred to this side as the high-concentration side and the other side as the low-concentration side. A typical simulation box of a $D_{pore} = 2$ nm membrane contained 68020 water molecules and 1840 Na+ and Cl⁻ ions, respectively. Each simulation box was equilibrated for 50 ns at 300 K in the NVT ensemble. After ions diffused across the membrane, we moved the ions on the low-concentration side of the membrane back to the high-concentration side of the box, while keeping the ions within the membrane in place. We then equilibrated the high-concentration side of the simulation box for 5 ns at 300 K in the NVT ensemble before we performed the ion-transport simulations. To compute the number of permeated ions N'(t) and

the Na⁺/Cl⁻ flux ratio, we ran five independent repetitions of each simulation condition and counted the numbers of Na⁺ and Cl⁻ ions, N'(t), that were transported across the membrane every 1 ns for the first 25 ns (Figure 4A inset). To avoid overcounting ions stabilized by the membrane, we excluded ions within 0.5 nm of the membrane. Note that we normalized the number of permeated ions N'(t) by the corresponding membrane area A. We fit a linear curve $N'(t) = R_{\rm ion} \cdot t$ to the data points obtained from these five repetitions and computed the Na⁺/Cl⁻ flux ratio as $R_{\rm Na}/R_{\rm Cl}$. The net number of permeated charges was computed as $Q = N'_{\rm Na}(t = 25 \text{ ns}) - N'_{\rm Cl}(t = 25 \text{ ns})$ (Figure S13). The ion density maps in Figure S11 were computed from the density of ions within the membrane for the five 25 ns simulations with $D_{\rm pore} = 2.25$ nm and $\theta_{\rm Cl} = 1.3$. The grid size was 0.1 nm in both directions. The density plot in Figure 1D was computed from the average ion density of all pores from the same simulation set.

ASSOCIATED CONTENT

5 Supporting Information

The Supporting Information is available free of charge at https://pubs.acs.org/doi/10.1021/jacs.2c12853.

Additional experimental details; and detailed characterization of the 2DNP membrane (PDF)

AUTHOR INFORMATION

Corresponding Author

Jiwoong Park — Department of Chemistry, University of Chicago, Chicago, Illinois 60637, United States; James Franck Institute and Pritzker School of Molecular Engineering, University of Chicago, Chicago, Illinois 60637, United States; Email: jwpark@uchicago.edu

Authors

Baorui Cheng — Department of Chemistry, University of Chicago, Chicago, Illinois 60637, United States;
orcid.org/0000-0003-0505-4385

Yu Zhong — Department of Chemistry, University of Chicago, Chicago, Illinois 60637, United States; Present Address: Department of Materials Science and Engineering, Cornell University; Ithaca, NY 14853, USA; orcid.org/0000-0001-8631-2213

Yuqing Qiu — Department of Chemistry, University of Chicago, Chicago, Illinois 60637, United States;
ocid.org/0000-0002-0745-3155

Suriyanarayanan Vaikuntanathan — Department of Chemistry, University of Chicago, Chicago, Illinois 60637, United States; James Franck Institute, University of Chicago, Chicago, Illinois 60637, United States; ⊚ orcid.org/0000-0003-2431-6045

Complete contact information is available at: https://pubs.acs.org/10.1021/jacs.2c12853

Author Contributions

"Y.Z and Y.Q contributed equally.

Notes

The authors declare no competing financial interest.

ACKNOWLEDGMENTS

This work was supported by the Air Force Office of Scientific Research (FA9550-16-1-0347, FA9550-18-1-0480, and FA9550-21-1-0323) and National Science Foundation (DMR-2011854 and DMR-1848306). B. Cheng acknowledges the support by the Anthony L. Turkevich Research Fellowship and the William Rainey Harper Dissertation Fellowship

through the University of Chicago. We thank C. Liu for helpful discussions and J. H. Yu for helping with the laser patterning experiments.

REFERENCES

- (1) Logan, B. E.; Elimelech, M. Membrane-based processes for sustainable power generation using water. *Nature* **2012**, *488*, 313–319.
- (2) Siria, A.; Bocquet, M. L.; Bocquet, L. New avenues for the large-scale harvesting of blue energy. *Nat. Rev. Chem.* **2017**, *1*, 0091.
- (3) Zhang, R.; et al. A Streaming Potential/Current-Based Microfluidic Direct Current Generator for Self-Powered Nanosystems. *Adv. Mater.* **2015**, *27*, 6482–6487.
- (4) Schroeder, T. B. H.; et al. An electric-eel-inspired soft power source from stacked hydrogels. *Nature* **2017**, *552*, 214–218.
- (5) Fu, Y.; Guo, X.; Wang, Y.; Wang, X.; Xue, J. An atomically-thin graphene reverse electrodialysis system for efficient energy harvesting from salinity gradient. *Nano Energy* **2019**, *57*, 783–790.
- (6) Yazda, K.; et al. High Osmotic Power Generation via Nanopore Arrays in Hybrid Hexagonal Boron Nitride/Silicon Nitride Membranes. *Nano Lett.* **2021**, 21, 4152–4159.
- (7) Wang, H.; et al. Blue Energy Conversion from Holey-Graphene-like Membranes with a High Density of Subnanometer Pores. *Nano Lett.* **2020**, *20*, 8634–8639.
- (8) Liu, X.; et al. Power generation by reverse electrodialysis in a single-layer nanoporous membrane made from core—rim polycyclic aromatic hydrocarbons. *Nat. Nanotechnol.* **2020**, *15*, 307–312.
- (9) Feng, J.; et al. Single-layer MoS2 nanopores as nanopower generators. *Nature* **2016**, *536*, 197–200.
- (10) Yang, J.; et al. Advancing osmotic power generation by covalent organic framework monolayer. *Nat. Nanotechnol.* **2022**, *17*, 622–628.
- (11) Cao, L.; et al. On the Origin of Ion Selectivity in Ultrathin Nanopores: Insights for Membrane-Scale Osmotic Energy Conversion. *Adv. Funct. Mater.* **2018**, 28, 1804189.
- (12) Wang, L.; Wang, Z.; Patel, S. K.; Lin, S.; Elimelech, M. Nanopore-Based Power Generation from Salinity Gradient: Why It Is Not Viable. *ACS Nano* **2021**, *15*, 4093–4107.
- (13) Heiranian, M.; Noh, Y.; Aluru, N. R. Dynamic and weak electric double layers in ultrathin nanopores. *J. Chem. Phys.* **2021**, *154*, 134703.
- (14) Gadaleta, A.; et al. Sub-additive ionic transport across arrays of solid-state nanopores. *Phys. Fluids* **2014**, *26*, 012005.
- (15) Nakayama, H. Solid-Liquid and Liquid-Liquid Phase Equilibria in the Symmetrical Tetraalkylammonium Halide—Water Systems. *Bull. Chem. Soc. Ipn.* **1981**, *54*, 3717—3722.
- (16) Yu, X.; et al. Gating Effects for Ion Transport in Three-Dimensional Functionalized Covalent Organic Frameworks. *Angew. Chem.* **2022**, 134, No. e202200820.
- (17) Quan, A.; et al. Cation-Gated Ion Transport at Nanometer Scale for Tunable Power Generation. *J. Phys. Chem. Lett.* **2022**, *13*, 2625–2631.
- (18) Zhang, Z.; et al. Cation-selective two-dimensional polyimine membranes for high-performance osmotic energy conversion. *Nat. Commun.* **2022**, *13*, 3935.
- (19) Xantheas, S. S. Quantitative description of hydrogen bonding in chloride-water clusters. *J. Phys. Chem.* **1996**, *100*, 9703–9713.
- (20) Yamdagni, R.; Kebarle, P. Hydrogen-Bonding Energies to Negative Ions from Gas-Phase Measurements of Ionic Equilibria. *J. Am. Chem. Soc.* **1971**, 93, 7139–7143.
- (21) Dzidic, I.; Kebarle, P. Hydration of the alkali ions in the gas phase. Enthalpies and entropies of reactions M+(H2O)n-1 + H2O = M+(H2O)n. J. Phys. Chem. 1970, 74, 1466–1474.
- (22) Dunbar, R. C. Metal cation binding to phenol: DFT comparison of the competing sites. J. Phys. Chem. A 2002, 106, 7328-7337.
- (23) Zhong, Y.; et al. Wafer-scale synthesis of monolayer two-dimensional porphyrin polymers for hybrid superlattices. *Science* **2019**, *366*, 1379–1384.

- (24) Siria, A.; et al. Giant osmotic energy conversion measured in a single transmembrane boron nitride nanotube. *Nature* **2013**, 494, 455–458.
- (25) Hou, S.; et al. Free-Standing Covalent Organic Framework Membrane for High-Efficiency Salinity Gradient Energy Conversion. *Angew. Chem., Int. Ed.* **2021**, *133*, 10013–10018.
- (26) Secchi, E.; Niguès, A.; Jubin, L.; Siria, A.; Bocquet, L. Scaling Behavior for Ionic Transport and its Fluctuations in Individual Carbon Nanotubes. *Phys. Rev. Lett.* **2016**, *116*, 154501.
- (27) Dwyer, T. M.; Adams, D. J.; Hille, B. The permeability of the endplate channel to organic cations in frog muscle. *J. Gen. Physiol.* **1980**, 75, 469–492.
- (28) Kim, D. K.; Duan, C.; Chen, Y. F.; Majumdar, A. Power generation from concentration gradient by reverse electrodialysis in ion-selective nanochannels. *Microfluid. Nanofluidics* **2010**, *9*, 1215–1224
- (29) Dash, D.; Kumar, S.; Mallika, C.; Mudali, U. K. New Data on Activity Coefficients of Potassium, Nitrate, and Chloride Ions in Aqueous Solutions of KNO 3 and KCl by Ion Selective Electrodes. *ISRN Chem. Eng.* **2012**, 2012, 730154.
- (30) Sahu, S.; Zwolak, M. Colloquium: Ionic phenomena in nanoscale pores through 2D materials. *Rev. Mod. Phys.* **2019**, *91*, 021004.
- (31) Le Tilly, V.; Sire, O.; Wong, P. T. T.; Alpert, B. pH dependence of hydrogen bond strengths in myoglobin α -helices. *Chem. Phys. Lett.* **1992**, 192, 62–64.
- (32) Wu, X.; et al. H-bond interactions between arsenite and deoxynucleotides at different pH values: A combined computational and experimental study. *Chemosphere* **2020**, *251*, 126395.
- (33) Zhang, Z.; et al. Oxidation promoted osmotic energy conversion in black phosphorus membranes. *Proc. Natl. Acad. Sci. U.S.A.* **2020**, *117*, 13959–13966.
- (34) Li, R.; Jiang, J.; Liu, Q.; Xie, Z.; Zhai, J. Hybrid nanochannel membrane based on polymer/MOF for high-performance salinity gradient power generation. *Nano Energy* **2018**, *53*, 643–649.
- (35) Hong, S.; et al. Two-Dimensional Ti3C2Tx MXene Membranes as Nanofluidic Osmotic Power Generators. *ACS Nano* **2019**, *13*, 8917–8925.
- (36) Balme, S.; Ma, T.; Balanzat, E.; Janot, J. M. Large osmotic energy harvesting from functionalized conical nanopore suitable for membrane applications. *J. Membr. Sci.* **2017**, *544*, 18–24.
- (37) Zhu, X.; et al. Unique ion rectification in hypersaline environment: A high-performance and sustainable power generator system. *Sci. Adv.* **2018**, *4*, No. eaau1665.
- (38) Zhang, Z.; et al. Engineered Asymmetric Heterogeneous Membrane: A Concentration-Gradient-Driven Energy Harvesting Device. *J. Am. Chem. Soc.* **2015**, *137*, 14765–14772.
- (39) Tsai, T. C.; Liu, C. W.; Yang, R. J. Power Generation by Reverse Electrodialysis in a Microfluidic Device with a Nafion Ion-Selective Membrane. *Micromachines* **2016**, *7*, 205.
- (40) DeMille, R. C.; Molinero, V. Coarse-grained ions without charges: Reproducing the solvation structure of NaCl in water using short-ranged potentials. *J. Chem. Phys.* **2009**, *131*, 034107.
- (41) Molinero, V.; Moore, E. B. Water modeled as an intermediate element between carbon and silicon. *J. Phys. Chem. B* **2009**, *113*, 4008–4016.
- (42) Huang, Z.; et al. Essence of the Enhanced Osmotic Energy Conversion in a Covalent Organic Framework Monolayer. *ACS Nano* **2022**, *16*, 17149.
- (43) Iftimie, R.; Minary, P.; Tuckerman, M. E. Ab initio molecular dynamics: Concepts, recent developments, and future trends. *Proc. Natl. Acad. Sci. U.S.A.* **2005**, *102*, 6654–6659.
- (44) Jiang, Z.; et al. Aligned macrocycle pores in ultrathin films for accurate molecular sieving. *Nature* **2022**, *609*, 58–64.
- (45) Cheng, C.; Iyengar, S. A.; Karnik, R. Molecular size-dependent subcontinuum solvent permeation and ultrafast nanofiltration across nanoporous graphene membranes. *Nat. Nanotechnol.* **2021**, *16*, 989–995.

- (46) Uliana, A. A.; et al. Ion-capture electrodialysis using multifunctional adsorptive membranes. *Science* **2021**, *372*, 296–299.
- (47) Zuo, X.; et al. Thermo-Osmotic Energy Conversion Enabled by Covalent-Organic-Framework Membranes with Record Output Power Density. *Angew. Chem., Int. Ed.* **2022**, *61*, No. e202116910.
- (48) Chen, S.; et al. Imparting Ion Selectivity to Covalent Organic Framework Membranes Usingde NovoAssembly for Blue Energy Harvesting. J. Am. Chem. Soc. 2021, 143, 9415–9422.
- (49) Plimpton, S. Fast parallel algorithms for short-range molecular dynamics. *J. Comput. Phys.* **1995**, *117*, 1–19.
- (50) Jorgensen, W. L.; Madura, J. D.; Swenson, C. J. Optimized Intermolecular Potential Functions for Liquid Hydrocarbons. *J. Am. Chem. Soc.* **1984**, *106*, 6638–6646.
- (51) Qiu, Y.; Molinero, V. Morphology of Liquid-Liquid Phase Separated Aerosols. J. Am. Chem. Soc. 2015, 137, 10642–10651.

□ Recommended by ACS

Porphyrin-Based Covalent Organic Frameworks Anchoring Au Single Atoms for Photocatalytic Nitrogen Fixation

Ting He, Yanli Zhao, et al.

MARCH 08, 2023

JOURNAL OF THE AMERICAN CHEMICAL SOCIETY

READ 🗹

Molecular-Engineered Biradicals Based on the Y^{III}-Phthalocyanine Platform

Nithin Suryadevara, Mario Ruben, et al.

JANUARY 19, 2023

JOURNAL OF THE AMERICAN CHEMICAL SOCIETY

READ 🗹

Coaxially Conductive Organic Wires Through Self-Assembly

Shayan Louie, Colin P. Nuckolls, et al.

FEBRUARY 28, 2023

JOURNAL OF THE AMERICAN CHEMICAL SOCIETY

READ 🗹

Cation-Templated Assembly of 6₁³ and 6₂³ Metalla-Links

Hai-Ning Zhang, Guo-Xin Jin, et al.

JANUARY 30, 2023

JOURNAL OF THE AMERICAN CHEMICAL SOCIETY

READ 🗹

Get More Suggestions >